Dynamic properties of attached eddies in transitioning boundary layers and developed turbulence

By A. Elnahhas, A. Lozano-Durán†‡, P. Moin AND J. M. Wallace¶

Park *et al.* (2012) and Sayadi *et al.* (2013) found that single-point statistics within regions in the late stages of boundary layer transition conditioned on the presence of elevated enstrophy match those of fully developed turbulence. Elnahhas *et al.* (2022) showed that, in an H-type transition scenario, the geometrical properties of the attached momentum-transfer structures rapidly converge to those of fully developed turbulence. This study extends these comparisons to the dynamical properties of the dominant momentum-carrying structures and the enstrophy-carrying vortex clusters. The structures identified at each instant are connected in time to form tracked spatiotemporal histories, allowing us to quantify their advection velocities, lifetimes, and birth and death locations. We find that both types of attached eddies have scaled advection velocities and lifetime distributions consistent with those found in fully developed turbulence early on in transition, and that the main difference between the transitional region and fully developed turbulence is the elevated birth and death probability densities, as well as the imbalance between them, in comparison to the fully developed turbulence steady-state probability densities.

1. Introduction

Many studies on turbulent spots (Emmons 1951; Cantwell *et al.* 1978; Henningson *et al.* 1987; Park *et al.* 2012; Marxen & Zaki 2019; Wu *et al.* 2020) and organized late-stage boundary layer transition, such as H-type transition (Sayadi *et al.* 2013), concluded that, conditioned on being within a local region of large enstrophy or wall-shear stress (i.e., a locally turbulent region), the primary single-point statistics of wall-bounded turbulent shear flows (i.e., the mean velocity profile, turbulence intensity and enstrophy distributions, and turbulent kinetic energy budgets) are recovered. These single-point statistics were extended to the geometrical properties of individual momentum-carrying structures by Elnahhas *et al.* (2022). Beyond these primarily kinematic statistics, the observation by Wu *et al.* (2017) of the existence of turbulent–turbulent spots (TUTS) deep within turbulent boundary layers, coupled with their apparent spatiotemporal similarity to transitional–turbulent spots (TRTS), provided further evidence that the underlying dynamics of the late stages of boundary layer transition and of fully developed turbulence are similar. However, Wu *et al.* (2017) did not quantify the dynamics of the structures evolving in the two flow regimes. That is the aim of this study.

The few studies focusing on coherent structures within TRTS and TUTS, rather than on their conditional single-point statistics, focused solely on visualizing and characterizing

† California Institute of Technology
‡ Massachusetts Institute of Technology
¶ University of Maryland, College Park

vortical structures indicative of the small scales of the flow (or their collective excitation). The reason for this focus is the coherent structure identification methods these studies used, which rely primarily on thresholding local quantities based on the velocity gradient tensor, such as its second invariant, the Q criterion (Hunt *et al.* 1988); its discriminant $\mathcal{D}$ (Chong *et al.* 1990); or the imaginary part of its complex eigenvalue, the swirling strength λ_{ci} (Adrian 2007). To ensure that we examine the dynamical similarities between large and small scales, in this study we explore the dynamics of structures responsible for transporting momentum within wall-bounded turbulent shear flows, as well as those of vortical structures.

The primary coherent structures that transport momentum across the turbulent wall layer, namely ejections and sweeps, were observed in seminal studies by Kline *et al.* (1967) and Corino & Brodkey (1969). The aggregate statistical characteristics of all these ejections and sweeps within a flow can be obtained by decomposing the streamwise and wall-normal velocity fluctuations into quadrants based on their sign combinations, as was first done by Wallace *et al.* (1972). By extending the standard quadrant analysis technique to three-dimensional connected regions in space, Lozano-Durán *et al.* (2012) extracted structural information about the momentum-carrying structures in fully developed turbulent channel flows, elucidating their spatial organization, characteristic scales, and geometric shapes. Del Álamo *et al.* (2006) did this first for vortex clusters in turbulent channel flow. Looking for spatial overlaps between structures identified from one time instance to the next allows the spatiotemporal history of an eddy to be stitched together into a graph (Lozano-Durán & Jiménez 2014). We construct and analyze such spatiotemporal graphs for momentum-carrying structures and vortex clusters in both the transitional and fully turbulent regions of a naturally transitioning H-type boundary layer to quantify how far upstream the dynamical properties of coherent structures converge to those of fully developed turbulence.

The rest of this paper is organized as follows. Section 2 describes the direct numerical simulation (DNS) transitioning boundary layer data used for the analysis. It summarizes the algorithm used to extract the momentum-carrying structures and vortex clusters and explains how to organize them into networks. Section 3 presents the statistical dynamical properties of momentum-carrying structures and vortex clusters. These statistics are conditioned on the downstream distance from the point of breakdown of the Λ vortices. Finally, Section 4 presents our conclusions.

2. Dataset and methodology

2.1. *Boundary layer properties and region partitioning*

We use a setup similar to that of Sayadi *et al.* (2013) to extract and analyze both eddy types, namely the momentum-carrying structures and vortex clusters. In this flow, x, y, and z correspond to the streamwise, wall-normal, and spanwise directions, respectively; U and u, V and v, and W and w are the corresponding total and fluctuating velocities in each direction; ν is the kinematic viscosity; U_∞ is the freestream velocity; and $u_\tau(x)$ is the spanwise-averaged, streamwise-dependent friction velocity. The DNS is simulated using a setup similar to setup b in the study by Lozano-Durán *et al.* (2018), where the nonlinear parabolized stability equations (PSE) are used to advance a Tollmien–Schlicting (TS) wave along with a subharmonic oblique mode from $Re_x = 1.8 \times 10^5$ to the inflow plane. The advanced disturbances are superposed on a Blasius boundary layer to complete the inlet boundary condition. The solver utilizes a staggered second-order spatial

L_x/δ_0	L_y/δ_0	L_z/δ_0	δ_{L_x}/δ_0	Δx^+	Δz^+	$\Delta y^+\|_{\min}$	$\Delta y^+\|_{\delta_{99}}$	T/T_{eddy}	Δt_K^+	Δt_D^+	N_K	N_D
194.6	17.5	18.5	4.1	9.8	7.1	0.34	18.0	34.3	23.1	1.15	600	12,000

TABLE 1. The simulation parameters. L_x, L_y, and L_z are domain extents in the streamwise, wall-normal, and spanwise directions, respectively. δ_{L_x} is the boundary layer thickness at the outlet of the simulation. All spatial parameters are normalized by the inlet boundary layer thickness, δ_0. Δx^+, Δy^+, and Δz^+ are the grid spacings in the streamwise, wall-normal, and spanwise directions, respectively, normalized by the viscous length scale, $\delta_\nu = \nu/u_\tau$ at $Re_\theta = 925$. T denotes the total simulation time, which is normalized by $T_{eddy} = \delta_{99}/u_\tau$, the characteristic eddy-turnover time at $Re_\theta = 925$. Δt^K and Δt^D denote the temporal spacing between snapshots used for the kinematic and dynamic analyses corresponding to N_K and N_D flow fields, respectively. Both timescales are normalized by viscous time units, $\tau_\nu = \nu/u_\tau^2$, at $Re_\theta = 925$.

discretization scheme with third-order Runge–Kutta time stepping. The nondimensional frequency of the TS wave is $2F = \omega\nu/U_\infty^2 = 1.2395 \times 10^{-4}$, and the frequency of the subharmonic mode is F. The spanwise wavenumber of the subharmonic mode normalized by the thickness of the Blasius boundary layer at $Re_x = 1.8 \times 10^5$, δ_0^{PSE}, is $\beta\delta_0^{\mathrm{PSE}} = 0.6888$. The actual DNS simulation domain begins at $Re_x = 3.90 \times 10^5$, and the boundary layer thickness at this inflow location, δ_0, is used to normalize the coordinates. Table 1 lists the extents of the domain in each direction; the exit boundary layer thickness, δ_{L_x}; the spatial resolution; and the temporal resolution at which snapshots are stored for both dynamic and kinematic analyses. Given the spanwise wavelength of the subharmonic mode, the spanwise extent of the domain is such that three wavelengths are accommodated precisely at the inlet.

Figure 1 shows time- *and* spanwise-averaged streamwise-varying properties such as the skin-friction coefficient, C_f; the momentum-thickness-based and friction Reynolds numbers, $Re_\theta = U_\infty\theta/\nu$ and $Re_\tau = u_\tau\delta_{99}/\nu$, respectively; and the boundary layer thickness, δ_{99}. Computing $\delta_{99}(x)$ and $U_\infty(x)$ utilizes the procedure presented by Griffin *et al.* (2021). Figure 2 shows an instantaneous snapshot of the near-wall streamwise velocity streaks at $y^+|_{Re_\theta=925} = 15$. To find where the boundary layer forgets about the periodic inlet boundary condition, Figure 1 depicts the difference between the instantaneous streamwise velocity and an artificial velocity field constructed by replicating a region of the flow whose width is one wavelength of a TS wave,

$$u^*(x, y, z, t) = u(x, y, z, t) - u_p(x, y, z, t), \tag{2.1}$$

where

$$u_p(x, y, z + nL_z/3, t) = u_p^*(x, y, z, t) \;\; \forall\; n \in [0, 1, 2], \tag{2.2}$$

and

$$u_p^*(x, y, z, t) = \{u(x, y, z, t) : z \in [0, L_z/3)\}. \tag{2.3}$$

The velocity u^* is substantial only once the turbulence has sufficiently forgotten its initial condition during the transition process. To better quantify the streamwise memory of the flow, we examine a dimensionless eddy-turnover distance, $\tilde{x}$, defined as

$$\tilde{x} = \int^x \frac{u_\tau(x')}{\delta_{99}(x')U_\infty(x')} dx', \tag{2.4}$$

which is a measure of the distance advected by an eddy due to the freestream velocity as it goes through overturning motions (Sillero *et al.* 2013). The origin chosen for this

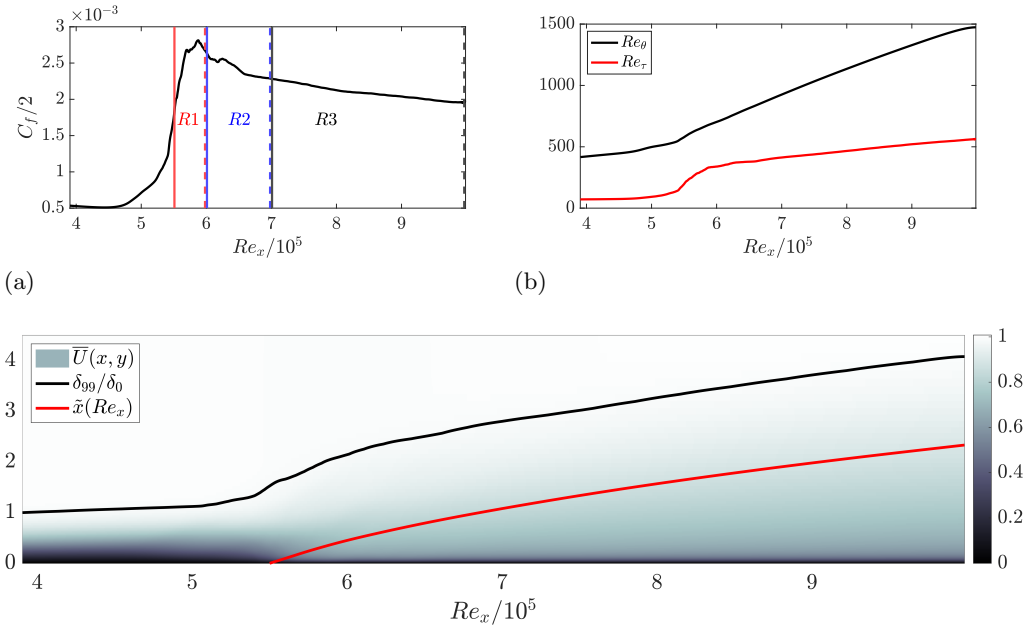

FIGURE 1. Streamwise-varying aggregate properties of the boundary layer. (a) The skin-friction coefficient. The vertical color-coded solid and dash-dotted lines mark the beginning and end of the three regions of the flow to be analyzed. (b) Re_θ and Re_τ. (c) $\delta_{99}(Re_x)$; the eddy-turnover length, $\tilde{x}(Re_x)$; and the mean streamwise velocity of the boundary layer.

quantity is the location where the Λ vortices first break down, estimated to be around $Re_x = 5.5 \times 10^5$. Figure 1(c) visualizes $\tilde{x}$. A comparison between Figures 1(c) and 2(b) indicates that turbulence loses the memory of its upstream transition process around $Re_x = 7{\times}10^5$, almost precisely after one eddy-turnover length as $\tilde{x}(Re_x = 7{\times}10^5) \approx 1.08$. $Re_x = 7 \times 10^5$ corresponds to $Re_\theta \approx 925$, which is consistent with the location at which one-point turbulence statistics collapse to those of fully developed turbulence, as per the observations by Sayadi *et al.* (2013). That is why we used this location to extract the reference length and timescales for normalization.

The domain is then partitioned into three regions to analyze the structural and dynamical properties of the eddies present in them. Region one ($R1$) starts at the breakdown of the Λ vortices and ends to the right of the skin-friction peak, covering the region of strong streamwise nonequilibrium, $\tilde{x} \in (0, 0.452]$. Region two ($R2$) includes the recovery region to the right of the skin-friction peak and ends at the location where turbulence loses memory of the transition mechanism, $\tilde{x} \in (0.452, 1.08]$. Region three ($R3$) covers the fully developed turbulence in the rest of the domain, $\tilde{x} \in (1.08, 2.34]$. The three regions are depicted in Figures 1(a) and 2(a).

2.2. *Coherent structure identification algorithm*

The clustering algorithm developed by Lozano-Durán *et al.* (2012) is adapted for a two-dimensional spatially varying mean flow field with a turbulent–nonturbulent interface (TNTI). At each point in space and time, the absolute instantaneous value of some quantity of interest, ϕ, is compared with a threshold, Φ, that could be streamwise and

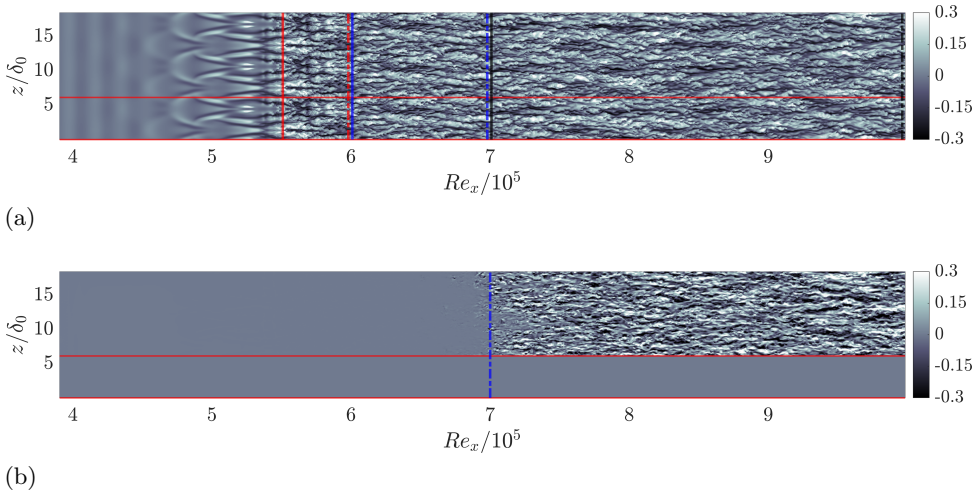

(a)

(b)

FIGURE 2. Near-wall streamwise streaks at $y^+_{925} = y^+(Re_\theta = 925) = 15$. (a) Total fluctuating velocity, $u(x, y^+_{925}, z)$. (b) Periodicity-subtracted velocity field, $u^*(x, y^+_{925}, z)$. The horizontal red lines mark the spanwise extent used to define $u^*_p(x, y, z)$. The vertical solid red line indicates the origin for the computation of $\tilde{x}$. The vertical dash-dotted blue line indicates the location at which turbulence loses memory of the upstream transition process. The vertical color-coded solid and dash-dotted lines are the same as those in Figure 1(a).

wall-normally varying, scaled by a constant, α_ϕ. For a single instant, a connected set of points, s_i, is defined as a single coherent structure. Each time instant contains many such connected sets of points, N_ϕ, whose union, $\mathcal{S}$, is defined as

$$\mathcal{S} = \bigcup_{i=1}^{N_\phi} s_i = \{(x, y, z) : |\phi| > \alpha_\phi \Phi\}. \tag{2.5}$$

To identify momentum-carrying structures, referred to as $\mathcal{M}$, we choose ϕ and Φ to be the instantaneous fluctuating turbulent stress, $\tau = uv$, and the local mean turbulence intensity product, respectively. To identify the vortex clusters, referred to as $\mathcal{V}$, we choose ϕ and Φ based on the instantaneous and root-mean-square values of the Q criterion of the fluctuating velocity gradient tensor instead of its discriminant (as in Del Álamo *et al.* 2006). The reason for this choice is that our simulation does not use a spectral code, which leads to strong aliasing errors when the discriminant is computed.

To complete the definition of instantaneous structures, we must account for the external nature of the flow, which introduces three complications. First, Φ goes to zero at the edge of the boundary layer, causing spuriously weak fluctuations to be highlighted as important structures. Second, as the edge of the boundary layer is approached, the variable used to define Φ requires intermittency corrections to reflect the correct strength of the turbulent fluctuations near the TNTI. Third, only structures that possess vorticity transported from the wall must be identified and distinguished from irrotational fluctuations due to entrainment. To remedy the first two issues, we adjust the thresholding field, Φ, as follows,

$$\Phi^*(x, y) = \begin{cases} \Phi(x, y) & \text{if } \; y/\delta_{99}(x) \le \ell, \\ \Phi(x, y/\delta_{99}(x) = \ell) & \text{if } \; y/\delta_{99}(x) > \ell, \end{cases} \tag{2.6}$$

where ℓ is a parameter chosen to select the region of the flow closest to the TNTI without strong intermittency corrections. Borrell & Jiménez (2016) showed that the intermittency parameter, $\gamma(y/\delta_{99})$, begins to decay rapidly around $y/\delta_{99} = 0.6$. Therefore, we set $\ell = 0.6$.

To address the third issue, we need an instantaneous approximation of the TNTI, which the structures must instantaneously lie below. To do so, we partly follow the process from Borrell & Jiménez (2016). In summary, we identify the viscously affected region of the flow and ignore the irrotational portion by thresholding the field of total vorticity magnitude $\omega = |\vec{\omega}|$ against a spatially varying threshold based on the expected vorticity fluctuations at the edge of the boundary layer. The resulting mask is adjusted slightly to ignore the turbulent droplets that detach into the freestream and the irrotational bubbles that break off into the turbulent region. The result is a slightly smoothed version of the instantaneously viscously affected region of the flow. The turbulent region, $\mathcal{T}$, is therefore defined as

$$\mathcal{T} = \overline{\left\{(x,y,z,t) : \omega > \alpha_\omega \frac{u_\tau^2(x)}{\nu(\delta_{99}^+(x))^{1/2}}\right\}}, \tag{2.7}$$

where the overline denotes the slight modifications of this set due to operations on turbulent droplets and nonturbulent bubbles, and $\alpha_\omega = 0.022$, per the analysis by Borrell & Jiménez (2016). This threshold is applied to the transitional portion of the boundary layer as well. The reader is referred to Borrell & Jiménez (2016) for the complete details.

The final definitions of the structures are

$$\mathcal{M} = \bigcup_{i=1}^{N_M} M_i = \{(x,y,z,t) : |\tau| > \alpha_M (u'(x,y)v'(x,y))^* \ \ \& \ \ (x,y,z,t) \in \mathcal{T}\}, \tag{2.8}$$

$$\mathcal{V} = \bigcup_{i=1}^{N_V} V_i = \{(x,y,z,t) : Q > \alpha_V (Q'(y))^* \ \ \& \ \ (x,y,z,t) \in \mathcal{T}\}, \tag{2.9}$$

where primed variables are root-mean-square quantities. A percolation analysis is performed to identify the scaling parameters of the spatially varying thresholds, α_M and α_V. The scaling parameters are chosen such that the average number of eddies of each type across time is maximized while simultaneously ensuring that no single eddy, s_i, contains the majority of the volume occupied by all eddies; in other words, we are simultaneously maximizing $\langle N_\phi \rangle$ and minimizing $\langle V(s_i)|_{max}/V(\mathcal{S})\rangle$. Figure 3 shows the results of the percolation analysis for the two eddy types, with chosen values of $(\alpha_M,\ \alpha_V) = (1.75, 2.00)$. During this process, α_ω was fixed. For all N_D and N_K flow fields analyzed, all α_ϕ were held constant.

For each coherent structure or cluster of points, s_i, henceforth referred to as eddies, volume-averaged quantities can be computed as

$$\Gamma_s = \frac{1}{V(s_i)} \int_{V(s_i)} \Gamma dV, \tag{2.10}$$

where $V(s_i)$ is the volume occupied by eddy s_i. Using this definition, and choosing Γ to be the streamwise and wall-normal velocities, we can define the eddy-averaged u_s and v_s. In the case of the momentum-transfer eddies, knowing these values allows us to associate the eddy with a particular Reynolds stress quadrant, where we focus on Q2 events ($u_s < 0, v_s > 0$) (ejections) and Q4 events (sweeps) ($u_s > 0, v_s < 0$). No subclassification is used for the vortex clusters based on eddy-averaged quantities. For

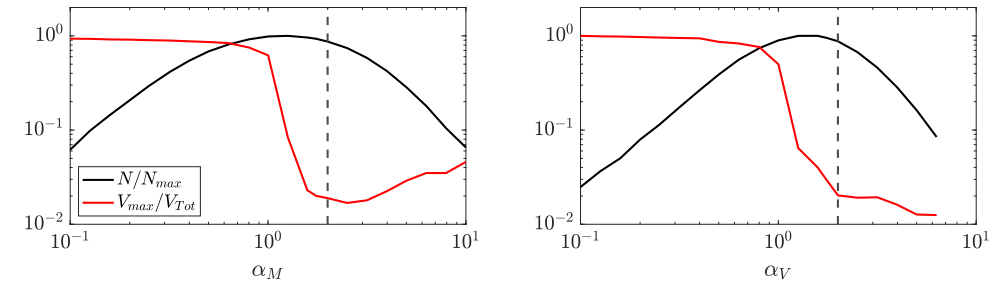

(a) (b)

FIGURE 3. Percolation analysis to identify the scaling of the thresholds for the two eddy types. (a) Momentum-transfer structures ($\mathcal{M}$). (c) Vortex clusters ($\mathcal{V}$). The vertical dashed gray lines indicate the final values chosen for α_M and α_V.

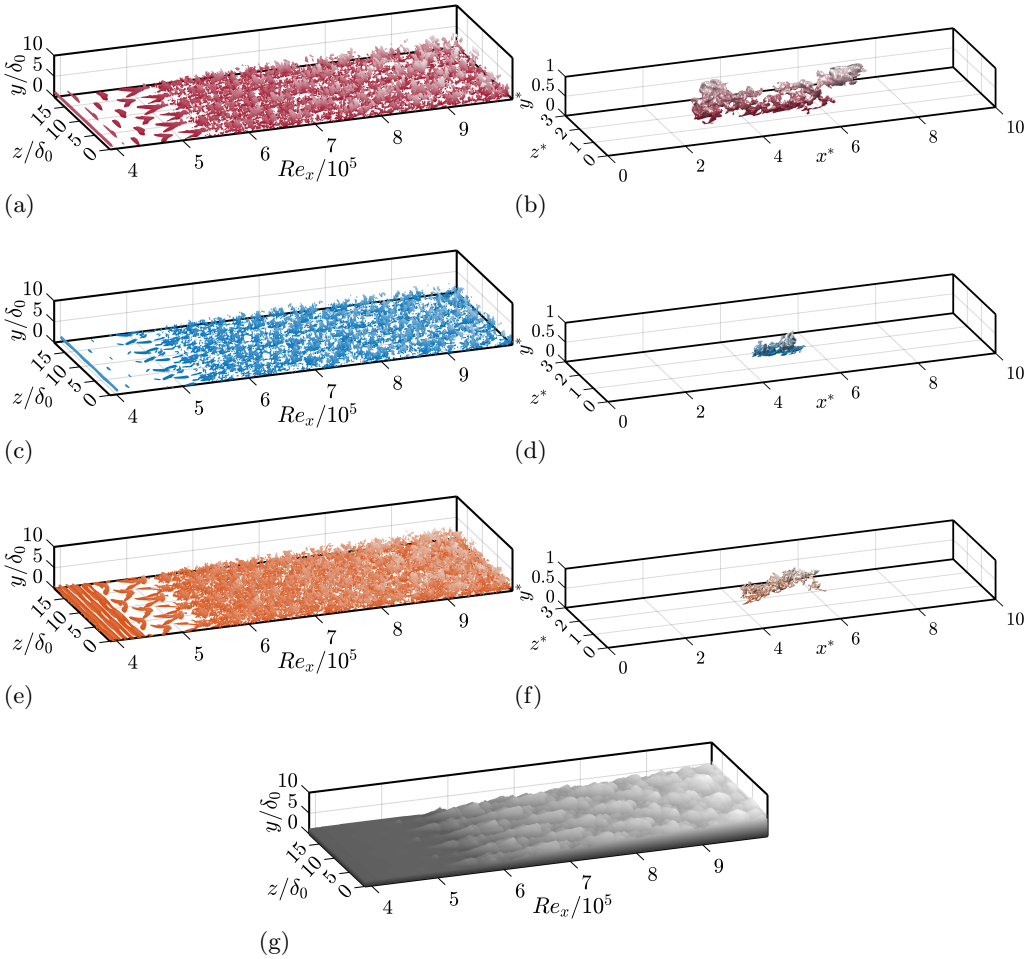

(a) (b)

(c) (d)

(e) (f)

(g)

FIGURE 4. Visualizations of the various types of eddies examined. (a,c,e,g) Full-domain visualizations. (b,d,f) The largest structures by volume of each type. The coordinates are normalized by the average boundary layer thickness at the location where they were extracted. (a,b) Ejections, Q2. (c,d) Sweeps, Q4. (e,f) Vortex clusters. (g) The instantaneous boundary layer, $\mathcal{T}$.

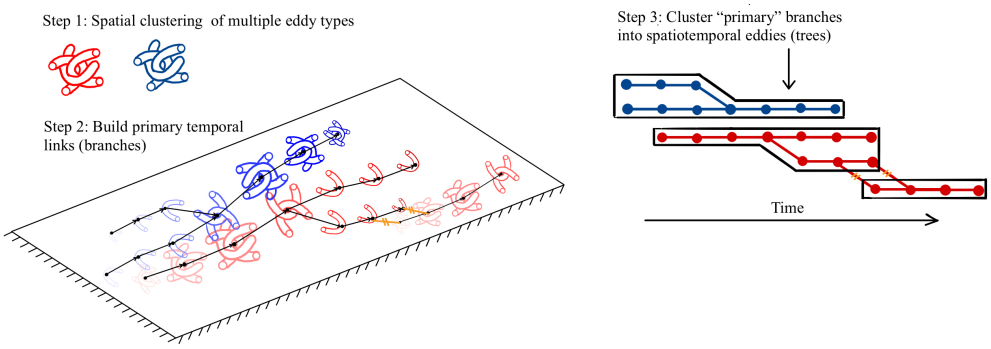

FIGURE 5. The spatiotemporal tracking algorithm. Lighter structures represent the same eddy earlier in its lifetime. Blue and red eddies correspond to an ejection–sweep pair occurring side by side. The crossed-out orange links represent intratype links between branches that were removed because they were not one another's primary links, resulting in the black polygons representing the spatiotemporal eddies defined in the text.

both eddy types, information such as their sizes, volumes, whether they are attached to the wall or not, advection velocities, and temporal lifetimes are extracted.

Figure 4(g) visualizes the instantaneous boundary layer in the entire domain as a scatter plot of the highlighted points in $\mathcal{T}$. Figure 4(a)-(f) highlights the different types of eddies embedded within this boundary layer as well as the largest individual structures in the domain of each type. The clustering algorithm with the spatially varying threshold identifies the important coherent structures in all regions of the flow before, during, and after transition. Signatures of the TS wave, the Λ vortices, their breakdown, and finally the fully turbulent structures are visible in the various eddy types examined. An interesting feature is that the algorithm detects the large-scale ejections and sweeps that are responsible for the large-scale structure of the TNTI.

2.3. *The spatiotemporal tracking algorithm*

Figure 5 shows the tracking algorithm. To track eddies in time, we cross-correlated the identified clusters from each pair of snapshots separated by Δt_D^+ of the same eddy type. The structures from the second snapshot are shifted backward in time by the two-dimensional streamwise and wall-normal mean velocities to account partially for their advection. Each of these clustering procedures results in connections from all N_B eddies to N_A eddies—that is, the number of eddies of the same type in the before (B) and after (A) snapshots. These connections are weighed by the relative volumetric overlap between the two connected eddies, defined as

$$O_{s_i^B \to s_j^A} = \frac{V(s_i^B \cap s_j^A)}{V(s_i^B)} \quad \text{and} \quad O_{s_j^A \to s_i^B} = \frac{V(s_i^B \cap s_j^A)}{V(s_j^A)}. \tag{2.11}$$

At this point, each pair of snapshots contains all the temporal links between structures. These correspond to each line segment separating two dots in Figure 5. This procedure is repeated for each eddy type. To construct the full spatiotemporal histories of eddies, the line segments must be clustered together.

First, temporal links between eddies of the same type that point to one another as the link with the maximum relative volumetric overlap are considered primary links—for example, if for s_*^B, the s_*^A for which $O_{s_*^B \to s_j^A}$ is maximum happens to maximize $O_{s_*^A \to s_j^B}$ for s_*^B. A recursive clustering of primary links results in branches, which are denoted

by horizontal collections of line segments in Figure 5. Branches are the spatiotemporal histories of individual eddies of each type. The first and final dots in a branch are labeled as its birth and death configurations.

A second clustering level can be established between branches of the same type, since branches can merge or split, as denoted by the diagonal line segments. This step is important because many small objects can detach and reattach to a large, central eddy. As such, branches that merge into or split from other branches at birth and death are clustered together with their parent branches, which could themselves be merging or splitting from other branches. This procedure is repeated recursively to construct graphs. During this second clustering step, there are two possibilities. First, there could be a single dominant branch with many small surrounding objects. If that is the case, no further steps are necessary. Second, multiple large eddies could appear simultaneously in time and end up clustered into the same graph because they are linked through smaller eddies. It would be preferable to consider multiple large eddies as individual events that interact. To do so, an extra step is performed during this second clustering procedure. We define primary interactions between branches analogously to how we defined them between eddies at two time steps, to break the graphs into subgraphs or trees (a collection of strongly interacting branches). This procedure is based on having two branches point to each other as having the largest relative volumetric overlap. However, unlike in the case of connecting eddies at two time steps, branches are spatiotemporal objects, and the relative volumetric overlap is computed by using the temporal history of each branch as follows,

$$O^b_{i\to j} = \frac{\int V^b_i \cap V^b_j dt_i}{\int V^b_i dt_i} \quad \text{and} \quad O^b_{j\to i} = \frac{\int V^b_j \cap V^b_i dt_j}{\int V^b_j dt_j}, \tag{2.12}$$

where the integration is over the lifetime of the source branch and V^b_i is the volume of a branch at a given time across its lifetime. The intersecting volume is computed at the same absolute time (with respect to the initial time of the simulation) for both branches. The branch link j to branch i with the highest overlap metric is considered the primary branch in the positive or negative time direction. Henceforth, we refer to the resulting subgraphs as spatiotemporal eddies, which are connected together in a network. This could result in graph partitioning, as indicated by the orange short strokes in Figure 5. Further details of the tracking algorithm can be found elsewhere (Lozano-Durán & Jiménez 2014; Bae & Lee 2021; Elnahhas *et al.* 2024).

3. Results and discussion

We now analyze the dynamical properties of the various types of momentum-carrying structures, which are also representative of the energy-carrying motions, and vortex clusters as a representation of the small scales of the flow.

First, we examine the birth and death probability density functions (PDFs) of eddies as a function of the boundary layer's local momentum thickness. We do so by tracking primary eddies using the algorithm presented in Figure 5 across their lifetimes and then recording their birth and death locations. Figure 6 presents these PDFs for all spatiotemporal ejections and sweeps, lumped together as momentum-transfer eddies, and vortex clusters attached to the wall at some time in their lives, defined as $\min_t y^+_{\rm bot}(t) \leq 20$, where $y^+_{\rm bot}(t)$ is the lowest point of the structures at a given time. The PDFs are also presented for those eddies that grow to be both attached and tall, where being tall is defined as having a maximum wall-normal extent, $\Delta^+_y(t) = y^+_{\rm top}(t) - y^+_{\rm bot}(t)$, at some point

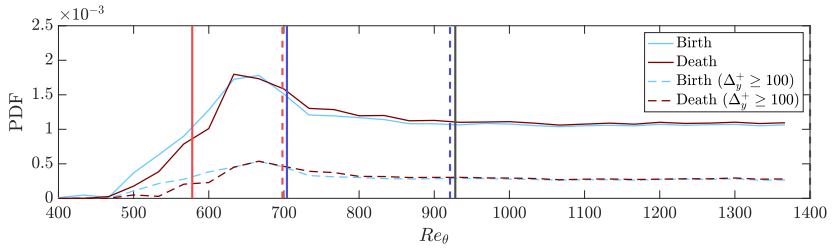

(a)

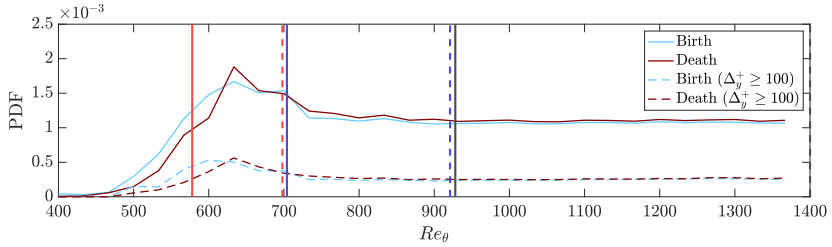

(b)

FIGURE 6. The birth and death PDFs of spatiotemporal eddies that at some time in their lives are attached; specifically, $y^+_{min}(t^*) < 20$ for some t^* in the eddy's life. The solid lines represent the results for all eddies, and the dashed lines represent the partial contributions to the PDFs resulting from the eddies that become tall. (a) Ejections and sweeps. (b) Vortex clusters.

across an eddy's lifetime of $\max_t \Delta_y^+(t) \geq 100$. We find that the birth and death PDFs peak during transition for both types of eddies and then settle toward a constant value at the beginning of $R3$. In the transition region, $R1$, the birth probability density exceeds the death probability density, as expected. In the recovery region, $R2$, the probability density of death slightly exceeds the probability density of birth, presumably because of the death of the excess eddies formed in $R1$. This trend is more cleanly observed when focusing on the partial contributions to the PDFs coming from the tall, attached eddies. The equilibrium values of the PDFs are reached immediately at the beginning of $R3$ around $Re_\theta \geq 925$. This equilibrium between the probabilities of births and deaths further explains why the turbulence statistics observed by Sayadi *et al.* (2013) collapse to those of fully developed turbulence around this Re_θ.

Figure 6 does not discern where eddies die with respect to their birth location. Figure 7 examines the birth and death joint PDF in terms of Re_θ for both primary momentum-transfer eddies and vortex clusters. Interestingly, there is a nonzero probability that structures die upstream of where they are born. This probability is constant across all regions of the flow. However, the probability that structures die a certain distance downstream is a function of both the size of the eddy and the region in which it was born. As expected, tall eddies are more likely to travel farther than smaller eddies and better illustrate the dependence of their marginal death location PDF on the birth Re_θ location, as the width of the PDF is narrower in the first region than in the fully turbulent third region. However, for both momentum-transfer events and vortex clusters, their marginal death location PDF asymptotes quite rapidly at the beginning of the second recovery region of the flow. Note that the ratio of the downstream widths of the marginal death PDF, measured as the difference between the 5% contour and the solid green line marking the origin, between the transitional and fully developed region ranges from 1.2 to

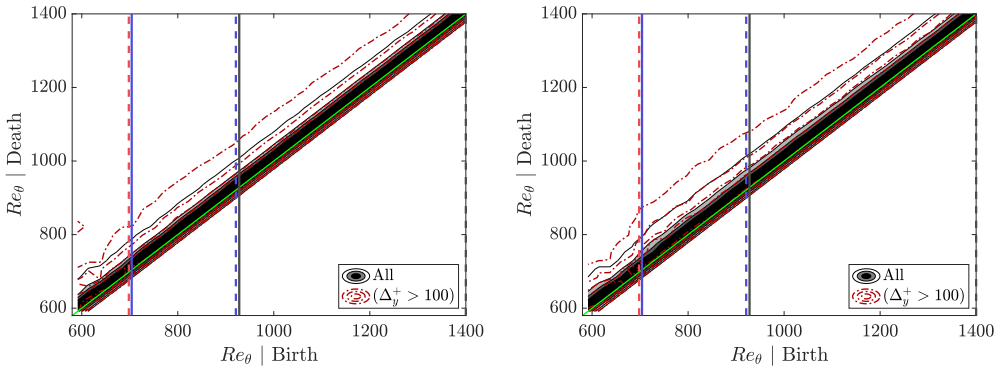

FIGURE 7. The birth and death location joint PDF with respect to the local Re_θ of the boundary layer for attached primary eddies. The solid-colored contours represent all attached eddies, while the dash-dotted contours represent tall, attached eddies. Both solid-colored and dash-dotted contours correspond to 5%, 25%, 50%, and 75% of the maximum of the marginal PDF at that Re_θ|Birth location. The solid green diagonal line corresponds to Re_θ|Death = Re_θ|Birth. The vertical lines demarcate the three regions of the flow. (a) Primary momentum-transfer eddies. (b) Vortex clusters.

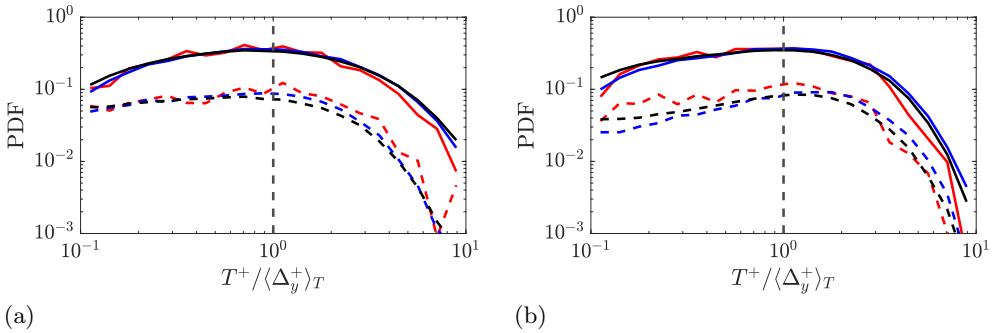

FIGURE 8. The PDF of the normalized lifetimes of the eddies within each region of the flow. Solid colors denote all eddies, and dashed lines denote the partial contributions to the lifetime PDFs coming from tall attached structures. (a) Ejections and sweeps. (b) Vortex clusters.

1.3. This ratio is close to the ratio of the peak of the friction velocities between the two regions, suggesting that the structures inhabiting the transition region travel shorter distances because their eddy-turnover times are faster than those in the fully developed region while maintaining equilibrium with their local mean shear environment. If eddies across all regions obey the same dynamical mechanisms—which we hypothesize is the case, given that their geometric properties are identical—an appropriate rescaling of their lifetimes with respect to their heights ($\Delta_y(t)$) and their local velocity scale (i.e., the local friction velocity u_τ) should collapse the PDFs of their lifetimes in inner units (T^+) across all regions. This is indeed the case in Figure 8, where the PDFs of the lifetimes of structures normalized using their local friction velocity and heights collapse across the three different flow regions for ejections and sweeps as well as vortex clusters.

We now examine the advection velocities of the attached eddies within the three re-

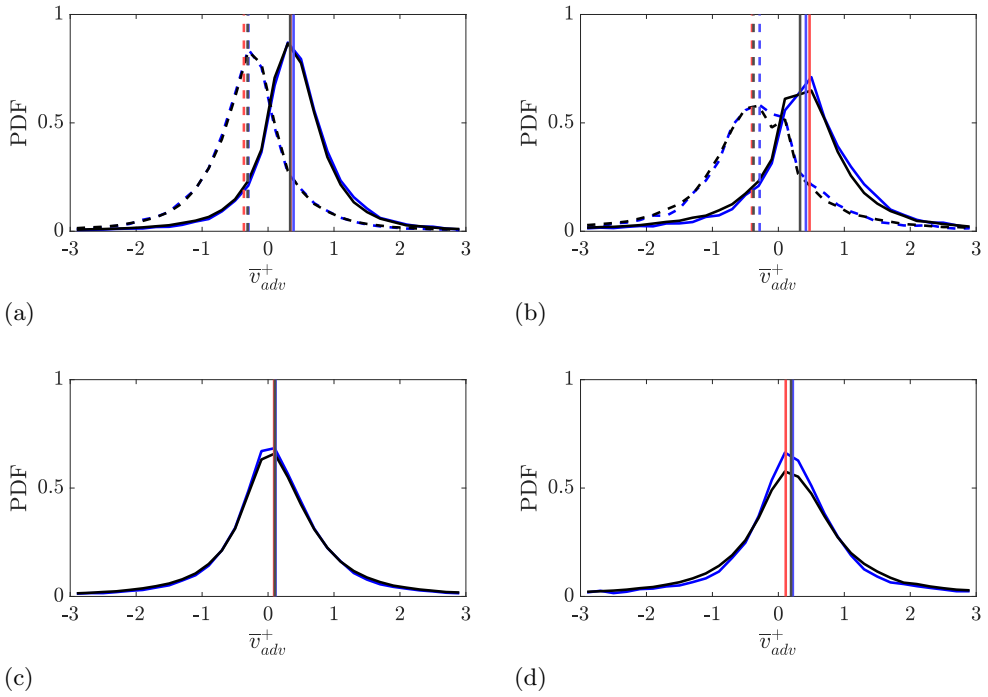

FIGURE 9. The PDF of the average wall-normal advection velocities throughout the lifetimes of each eddy. The lines are colored according to the three different regions of the flow. (a) Solid lines correspond to ejections, and dashed lines correspond to sweeps. The vertical lines denote the means of the samples and PDFs. (b) Conditioned on being tall momentum-transfer structures. (c,d) Vortex clusters depicting (c) all and (d) tall structures.

gions, defined as the velocity of their centroids in time. Figures 9 and 10 depict the average wall-normal and streamwise advection velocities of eddies throughout their lifetimes, normalized by the local friction velocity at their centroids at each instant in time. The average streamwise velocity would be defined as follows

$$\overline{u}^+_{adv} = \frac{1}{T}\int_0^T \frac{u_{adv}(t)}{u_\tau(x_c(t))}dt. \tag{3.1}$$

Note that for $R1$ the number of structures was insufficient to converge the PDFs within all bins at the same resolution as for $R2$ and $R3$, even though their coarsened versions do resemble those of $R2$ and $R3$. As such, we compare only the means from $R1$ in Figures 9 and 10. All means are denoted with vertical lines in both figures. We present both the PDFs of all attached structures and those extracted only from the tall ones.

We find that the wall-normal advection velocities of ejections and sweeps are approximately symmetric around zero, with the maximums of their PDFs centralized around their means ($\overline{v}^+_{adv} = \pm 0.35 \sim 0.4$). This symmetry indicates that they are likely parts of the same streamwise roller structures discussed by Lozano-Durán & Jiménez (2014). Vortex clusters are centralized around zero. For ejections and sweeps as well as vortex clusters, their PDFs converge in $R2$ and $R3$ and the means match in all three regions, again highlighting the rapid collapse of eddies into the turbulent phenomenology. The streamwise advection velocity of eddies again splits into faster-moving sweeps and slower-

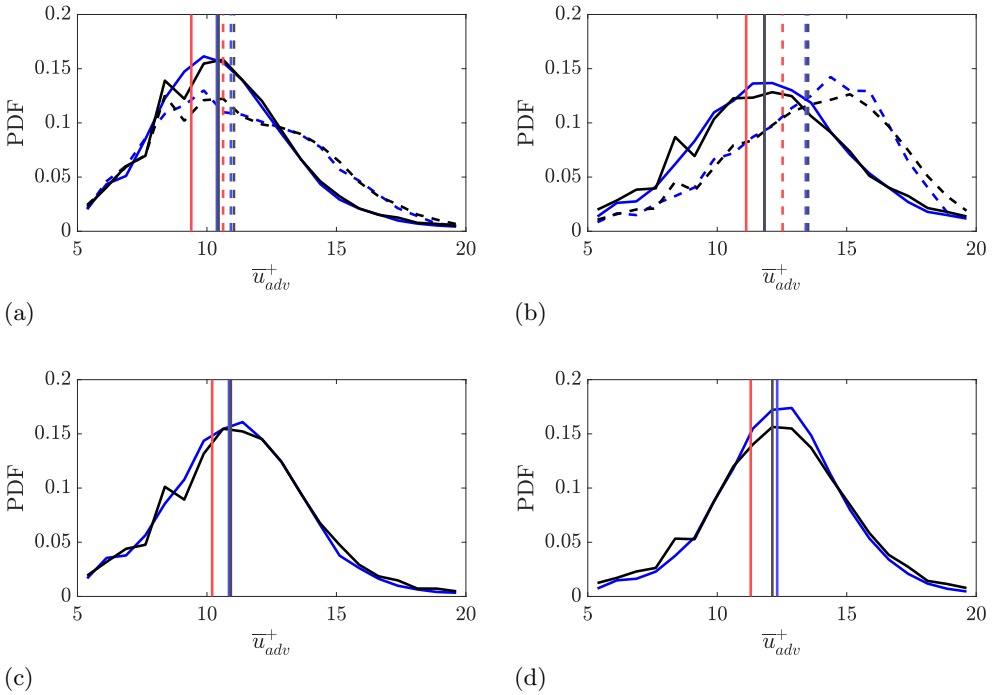

FIGURE 10. The PDF of the average streamwise advection velocities throughout the lifetime of each eddy. The lines are colored according to the three different regions of the flow. (a,b) Momentum-transfer eddies. Solid lines correspond to ejections, and dashed lines correspond to sweeps. The vertical lines correspond to the means of the samples and PDFs. (c,d) Vortex clusters. (a,c) PDFs of all attached eddies. (b,d) PDFs of all tall attached eddies.

moving ejections that are symmetric around $\overline{u}^+_{adv} \approx 13.5$. However, this symmetry appears only once eddies that are not tall are filtered out, as shown in Figure 10(b). The peaks in the PDF in Figure 10(a) at lower advection velocities are therefore the result of the smaller buffer layer structures, which advect with a constant velocity $\overline{u}^+_{adv} \approx 10$ set by the mean velocity at the bottom of the logarithmic region of the flow (as in Lozano-Durán & Jiménez 2014). The means of $R2$ and $R3$ approximately coincide, while those of $R1$ are consistently slower. The advection velocities of the vortex clusters match those of the ejections when either all eddies or only tall eddies are included, further indicating that they are housed within them.

4. Conclusions

Motivated by observations that conditional turbulent statistics far upstream in transitional turbulent boundary layers resemble those of fully developed turbulence, this study aimed to extend this comparison beyond single-point statistics to the dynamic properties of the dominant attached eddies of the flow. To ensure that our understanding was not limited to a single flow scale or biased by examining a single flow quantity, we simultaneously examined momentum-carrying structures, which are also representative of large energy-carrying motions, and vortex clusters, which represent the collective excitation of small, dissipative scales and serve as markers for the TRTS and TUTS of Wu *et al.*

(2017). To this end, we adapted the clustering algorithm used by Lozano-Durán *et al.* (2012) to extract the connected regions in space belonging to the different eddy types, and we adapted the temporal tracking algorithm used by Lozano-Durán & Jiménez (2014) to extract their evolution and analyze their dynamical properties. Focusing our analysis on the attached eddies present in the flow, we found that the statistical dynamical properties of these attached structures collapsed to the statistics observed in the fully developed region of the flow very rapidly upstream in $R1$, ahead of the peak in the skin-friction coefficient. We also found that the average lifetimes normalized by size, wall-normal, and streamwise advection velocities all collapse downstream of the breakdown of the Λ vortices. The main difference in the dynamic properties of the flow between the transitional and fully developed turbulence region is the imbalance in the probabilities at which new structures are born and die during transition, both of which are elevated before settling toward their fully turbulent equilibrium values at $Re_\theta \geq 925$.

Combining the results of this study with those of Elnahhas *et al.* (2022), we have shown that the similarity between early transitional boundary layers and fully developed turbulent wall-bounded flows extends beyond standard statistics, such as the mean velocity profile and turbulent intensities, to all basic geometrical and dynamic properties of the underlying attached eddies. It is remarkable how far upstream after the breakdown of discrete Λ vortices the collapse in all statistical measures hold, as they take less than one-half of an eddy-turnover length to emerge. This conclusion held for both large energy-carrying structures and those indicating the collective excitation of the small, dissipative scales of motion, namely vortex clusters.

Acknowledgments

A. E. and P. M. acknowledge support from NASA Transformation Tools and Technologies under grant 80NSSC20M0201. The geometrical and kinematic analysis, published in the Proceedings of the 18th Summer Program of the Center for Turbulence Research in 2022, was conducted using a preliminary version of the simulation used here. The authors thank Dr. Salvador Gomez for his insightful comments.

REFERENCES

Adrian, R. J. 2007 Hairpin vortex organization in wall turbulence. *Phys. Fluids* **19**, 041301.

Bae, H. J. & Lee, M. 2021 Life cycle of streaks in the buffer layer of wall-bounded turbulence. *Phys. Rev. Fluids* **6**, 064603.

Borrell, G. & Jiménez, J. 2016 Properties of the turbulent/non-turbulent interface in boundary layers. *J. Fluid Mech.* **801**, 554–596.

Cantwell, B., Coles, D. & Dimotakis, P. 1978 Structure and entrainment in the plane of symmetry of a turbulent spot. *J. Fluid Mech.* **87**, 641–672.

Chong, M. S., Perry, A. E. & Cantwell, B. J. 1990 A general classification of three-dimensional flow fields. *Phys. Fluids A* **2**, 765–777.

Corino, E. R. & Brodkey, R. S. 1969 A visual investigation of the wall region in turbulent flow. *J. Fluid Mech.* **37**, 1–30.

Del Álamo, J. C., Jiménez, J., Zandonade, P. & Moser, R. D. 2006 Self-similar vortex clusters in the turbulent logarithmic region. *J. Fluid Mech.* **561**, 329–358.

Elnahhas, A., Lenz, E., Moin, P., Lozano-Durán, A. & Bae, H. J. 2024 Are

the dynamics of wall turbulence in minimal channels and larger domain channels equivalent? A graph-theoretic approach. *J. Phys.: Conf. Ser.* **2753**(1), 012004.

Elnahhas, A., Lozano-Durán, A. & Wallace, J. 2022 A geometrical comparison of the momentum-carrying structures between boundary layer transition and fully developed turbulence. *Proceedings of the Summer Program*, Center for Turbulence Research, Stanford University, pp. 323–333.

Emmons, H. W. 1951 The laminar-turbulent transition in a boundary layer. Part I. *J. Aeronaut. Sci.* **18**, 490–498.

Griffin, K. P., Fu, L. & Moin, P. 2021 General method for determining the boundary layer thickness in nonequilibrium flows. *Phys. Rev. Fluids* **6**, 024608.

Henningson, D., Spalart, P. & Kim, J. 1987 Numerical simulations of turbulent spots in plane Poiseuille and boundary-layer flow. *Phys. Fluids* **30**, 2914–2917.

Hunt, J. C. R., Wray, A. A. & Moin, P. 1988 Eddies, streams, and convergence zones in turbulent flows. *Proceedings of the Summer Program*, Center for Turbulence Research, Stanford University, pp. 193–208.

Kline, S. J., Reynolds, W. C., Schraub, F. A. & Runstadler, P. W. 1967 The structure of turbulent boundary layers. *J. Fluid Mech.* **30**, 741–773.

Lozano-Durán, A., Flores, O. & Jiménez, J. 2012 The three-dimensional structure of momentum transfer in turbulent channels. *J. Fluid Mech.* **694**, 100–130.

Lozano-Durán, A., Hack, M. J. P. & Moin, P. 2018 Modeling boundary-layer transition in direct and large-eddy simulations using parabolized stability equations. *Phys. Rev. Fluids* **3**, 023901.

Lozano-Durán, A. & Jiménez, J. 2014 Time-resolved evolution of coherent structures in turbulent channels: characterization of eddies and cascades. *J. Fluid Mech.* **759**, 432–471.

Marxen, O. & Zaki, T. A. 2019 Turbulence in intermittent transitional boundary layers and in turbulence spots. *J. Fluid Mech.* **860**, 350–383.

Park, G. I., Wallace, J. M., Wu, X. & Moin, P. 2012 Boundary layer turbulence in transitional and developed states. *Phys. Fluids* **24**, 035105.

Sayadi, T., Hamman, C. W. & Moin, P. 2013 Direct numerical simulation of complete H-type and K-type transitions with implications for the dynamics of turbulent boundary layers. *J. Fluid Mech.* **724**, 480–509.

Sillero, J. A., Jiménez, J. & Moser, R. D. 2013 One-point statistics for turbulent wall-bounded flows at Reynolds numbers up to $\delta^+ \approx 2000$. *Phys. Fluids* **25**, 105102.

Wallace, J. M., Eckelmann, H. & Brodkey, R. S. 1972 The wall region in turbulent shear flow. *J. Fluid Mech.* **54**, 39–48.

Wu, X., Moin, P., Wallace, J. M., Skarda, J., Lozano-Durán, A. & Hickey, J.-P. 2017 Transitional–turbulent spots and turbulent–turbulent spots in boundary layers. *Proc. Natl. Acad. Sci. USA* **114**, E5292–E5299.

Wu, Z., Zaki, T. A. & Meneveau, C. 2020 High-Reynolds-number fractal signature of nascent turbulence during transition. *Proc. Natl. Acad. Sci. USA* **117**, 3461–3468.